Force redistribution during clathrin-mediated endocytosis revealed by new phase-separating force sensors

Yuan Ren[a,b], Jie Yang[c], Huaizhou Jin[c], Yongli Zhang[a,c,§], Julien Berro[a,b,c,§]

[a] Department of Molecular Biophysics and Biochemistry, Nanobiology Institute, Yale University, New Haven, CT, USA
[b] Nanobiology Institute, Yale University, West Haven, CT 06516, USA
[c] Department of Cell Biology, Yale University School of Medicine, New Haven, CT 06520, USA
[§] Contacts: julien.berro@yale.edu and yongli.zhang@yale.edu

Abstract:

Forces exerted at the molecular level are central to countless processes in health and disease. However, measuring molecular forces remains difficult if not impossible using existing approaches. During clathrin-mediated endocytosis (CME), the plasma membrane is deformed into a vesicle by the forces produced by the actin cytoskeleton and transmitted to the membrane by a multi-protein coat[1–3]. However, the actual forces required for endocytosis remain unknown. Here we present a new series of *in vivo* force sensors to measure the forces on the fission yeast HIP1R homologue End4p, a protein that links the endocytic membrane to the actin cytoskeleton[2,4]. These new force sensors are based on calibrated coiled-coils that phase separate when they are under force. The measured forces on End4p are between 11 and 20 pN near the actin meshwork, between 10 and 11 pN near the clathrin lattice, and between 8 and 10 pN near the plasma membrane. Our results predict the participation of additional proteins to relay forces in different layers of the endocytic machinery during CME, and our approach points to a novel direction for *in vivo* force measurement.

Main:

Extracellular materials are transported into cells via endocytosis. In eukaryotic cells, clathrin-mediated endocytosis (CME) is the major internalization pathway for nutrients, signaling molecules and pathogenic agents[5,6]. It is implicated in numerous diseases including cancer, neurological disorders and virus entry, and is therefore the focus for both basic and translational research[7,8]. The distinctive feature of CME is a layer of proteinaceous coat, of which clathrin is a prominent member. The coat contains more than 20 evolutionarily conserved proteins that assemble at the intracellular side of the endocytic site, curves as the endocytic pit matures, and disassembles after the budding of the endocytic vesicle[1,9]. Endocytic coat proteins make extensive interactions with each other, with the lipids of the plasma membrane, and with a meshwork of actin filaments that surrounds the endocytic coat[2–4,10–12]. Forces produced by actin polymerization are transmitted through adaptor proteins of the endocytic coat to help transform a flat membrane patch into a cargo-filled vesicle into the cytoplasm[2,12,13] (Fig. 1a).

Deformation of the membrane during CME is energetically expensive[13–15]. In mammalian cells with elevated membrane tension and in yeast cells where the turgor pressure is as high as 1 MPa, actin polymerization is required for successful CME[1,15,16]. Epsins and Hip1R are believed to transmit the force produced by actin assembly to the plasma membrane because their removal

stalls the invagination of endocytic pits, and their C-terminal domains (ACB and THATCH, respectively) bind actin filaments and their N-terminal domains (ENTH and ANTH, respectively) bind PIP2 on the membrane[2,10,12,17] (Fig. 1b). Because both proteins also bind clathrin and other endocytic coat proteins, it is possible that forces could be transmitted to the membrane via multiple routes[3,18–20]. In contrast to the abundant knowledge gained from biochemical and genetic approaches, a quantitative understanding of force production and distribution at the molecular level during CME is lacking, because tools to measure forces in live cells in the context of small (~ 100-nm diameter) and transient (~10 s) endocytic pits are scarce, difficult to use, and often too bulky to insert into proteins without causing side effects. Here we present a new approach for force measurement *in vivo* that overcomes these limitations.

The assembly of the endocytic coat relies on weak and multivalent interactions that facilitate the rapid exchange of binding partners during the dynamic rearrangement of the endocytic coat and the constant change in membrane shape during CME[21–23]. Many endocytic proteins contain promiscuous binding sites, multiple copies of short peptide motifs, and intrinsically disordered regions (IDRs)[4,11,21,22,24]. Recent developments in protein engineering have indicated that the dual incorporation of IDRs and oligomerization domains (either controlled by light or small molecules) promotes the phase separation of proteins *in vivo*[25–27]. We reasoned that if a mechanically actuated oligomerization domain is introduced into an endocytic adaptor protein that contains an IDR, protein phase separation could be induced in a force-dependent manner. The force required to activate this domain for oligomerization could be determined through calibration, and the formation of protein condensates would inform us of the presence of force.

Dimeric coiled-coils are excellent candidates for such mechanically actuated oligomerization domain, because they are small, have well-characterized mechanical properties, and can be easily introduced into proteins without affecting their normal functions[28–30] (Fig. S3a). We and others have previously measured the unfolding forces and energies of dimeric coiled-coils, and found that they unfold at pulling force thresholds in the range of 2-14 piconewtons (pN)[31–33]. The unfolding of a coiled-coil exposes two hydrophobic interaction surfaces that can mediate higher order oligomerization[34,35] (Fig. S3b, e). Therefore, we used this property to repurpose dimeric coiled-coils as *in vivo* force sensors.

First, we linked the two parallel α-helices in a heterodimeric GCN4 leucine zipper with a 30-amino acid flexible linker to form a single chain polypeptide that can be genetically encoded (Fig. S3a). To measure its unfolding force using optical tweezers, a single GCN4 coiled-coil was tethered between two beads held in two optical traps (Fig. 1c) and pulled to high force by separating the two traps at a speed of 10 nm/s[32]. Unfolding of the coiled-coil was manifested by a sudden extension increase at ~11 pN (Fig. 1d, black trace). The unfolded coiled-coil refolded during relaxation, but at a lower force (Fig. 1d, red trace). Repeated pulling and relaxation reveals a distribution of unfolding forces, with a single peak at 10.8 ± 0.4 pN (Mean ± SEM) (Fig. 1e). This coiled-coil is referred to as cc-11pN hereafter.

We inserted cc-11pN into the fission yeast homolog of Hip1R (End4p) at its genomic locus using CRISPR/Cas9 so that the expression level of End4p was not perturbed. End4p functions as a dimer *in vivo*[2,36], and contains an IDR between its proline rich domain and its dimerization domain (Fig. S1). In wild-type cells, fluorescently tagged End4p is present at endocytic sites and appear as diffraction-limited puncta (hereafter referred to as End4p patches) that are enriched at cell tips during interphase and around the division plane during mitosis (Fig. 1f, S2a, movie1,

S4c). When cc-11pN was inserted before the actin-binding THATCH domain of End4p, many large spherical End4p condensates appeared among small patches (Fig. 1g, 4Sf). The condensates remained visible in the cell during the entire time course of the movies (>10 min) whereas End4p remained at endocytic patches for a much shorter time (~ 50 seconds). Interestingly, the condensates displayed liquid-like features such as fusion and fission (Fig. 1h, S2b-c, movies 2-3).

We hypothesized that condensate assembly of End4p constructs is mediated by force-induced unfolding of cc-11pN, which in turn leads to the formation of inter-molecular association of the unfolded α-helices (Fig. 2a, S3e). To test this hypothesis, we created a construct where we shortened the linker between the two α-helices of cc-11pN to force the coiled-coil to be unfolded (Fig. S3c-d). Indeed, we observed larger condensates (Fig. 2b, S4), supporting our hypothesis that the unfolded coiled coils mediate the condensate assembly.

We constructed several control strains to demonstrate that the formation of End4p condensates is indeed force dependent. To remove the force on cc-11pN, we inserted it at the C-terminal of End4p (Fig. 2c), deleted the THATCH domain (Fig. 2d) or split the construct after the dimerization domain of End4p using the self-cleaving 2A peptide (Fig. 2e). We did not observe any condensate in the three cases, suggesting that the incorporation of cc-11pN *per se* does not cause End4p condensation, and that force is needed to generate End4p condensates. In all these experiments, the cellular localization of these End4p constructs was the same with or without the insertion of cc-11pN (Fig. S5a, S5b). Splitting cc-11pN between the two α-helices prohibited the formation of intermolecular coiled-coils, and thereby prevented the formation of End4p condensates (Fig. 2f, S3f). Mutations in the THATCH domain (R1093G in Fig. 2g, RVK1010DDD in Fig. 2h) that abolish the binding of End4p to F-actin also prevented the formation of End4p condensates[37,38]. Here too we controlled that the insertion of cc-11pN did not change the localization of End4p (Fig. S5d, S5e). Last, by inhibiting the polymerization of F-actin through Latrunculin A (LatA), we observed a reduction in both the size and the number of End4p condensates (Fig. 2i-k), demonstrating that the formation of End4p condensates depends on F-actin polymerization. Collectively, our data are consistent with the idea that force induced unfolding of cc-11pN in End4p promotes the phase separation of End4p constructs, and that the magnitude of force between End4p's dimerization and THATCH domain is above 11 pN.

To further assess the force involved in the condensate assembly, we designed and tested three more force sensors (based on artificial coiled-coils[39,40] and a B-ZIP protein[41]) (Fig. 3a-d) with average unfolding force thresholds of 8.2 ± 0.2 pN, 10.0 ± 0.1 pN and 20.0 ± 0.7 pN, which are hereafter referred to as cc-8pN, cc-10pN and cc-20pN respectively (Fig. 3e, Fig. S6a-c). The insertion of these three coiled-coils into actin-binding defective End4p did not lead to the formation of End4p condensates (Fig. S6d-f), and the insertion of these force sensors into the same position as cc-11pN showed that the magnitude of force before the THATCH domain is 11-20 pN (Figure 4a, right column).

This library of calibrated coiled-coil force sensors not only allowed us to refine our force measurements before the THATCH domain but also to measure the force at two other locations on End4p (Fig. 4a, S1a). The coiled-coil force sensors were inserted after the lipid-binding ANTH domain (Fig. 4a, left column), between the proline rich domain and the dimerization domain (Fig. 4a, middle column), or before the THATCH domain (Fig. 4a, right column). The insertion of the same coiled-coil at different locations led to End4p condensates in some but not

all cases (compare each row in Fig. 4a). Because the formation of End4p condensates reflects the local presence of force above the unfolding force threshold of the coiled-coil force sensors, our results demonstrate a gradient in the magnitude of force along End4p molecule: between 8 and 10 pN after the ANTH domain, between 10 and 11 pN between the proline rich domain and the dimerization domain, and between 11 and 20 pN before the THATCH domain.

The gradient of force on End4p suggests that the binding of other endocytic coat proteins to End4p dissipates the force transmitted from F-actin to the lipid membrane. We demonstrated this hypothesis by splitting End4p after its proline rich domain, therefore disconnecting End4p N-terminal from its C-terminal, but preserving the localization of End4p C-terminal at endocytic patches (Fig. S5c). Despite its inability to bind lipid, forces on End4p C-terminal were still large enough to unfold cc-11pN, confirming that forces are also transmitted to End4p via its binding partners in the endocytic coat (Fig. 4b). In the same vein, when we mutated the THATCH domain to prevent the direct binding between End4p and F-actin, we still measured forces higher than 8 pN between End4p's ANTH and proline rich domains, while forces after the proline rich domain were now smaller than 8 pN (Fig. 4c, 4d). This result clearly shows that other endocytic coat proteins mediate the transmission of force to the N-terminal of End4p, even when End4p itself is unable to bind F-actin. Taken together, these results demonstrate that, contrary to the common belief, forces are not transmitted solely through adaptor proteins such as End4p but are relayed and redistributed by End4p and its binding partners along the different layers of the endocytic coat.

Discussion:

Force requirement in CME has been the subject of multiple theoretical work, but direct force measurements in the densely woven coat of CME have been lacking[13,42,43]. Only one recent unpublished study in *S. cerevisiae* used FRET-based force sensors to measure the forces on the budding yeast homolog of End4p, Sla2, in a mutant background[36]. This study measured forces larger than 8 pN near the THATCH actin-binding domain. In our study, we developed calibrated coiled-coils as novel force sensors to induce force-dependent phase separation of the endocytic adaptor End4p, and discovered that, in a wild-type background, the forces directly transmitted by the actin network to End4p C-terminal end are between 11 and 20 pN. We also showed that there is a gradient of force along End4p, demonstrating forces are relayed and redistributed across the endocytic coat.

Our new strategy to measure forces in live cells harnesses the pre-existing multivalent interactions in protein complexes and circumvents the need for inserting two large fluorescent proteins in the middle of the target protein as prescribed in approached using FRET force sensors. Our force sensors are significantly smaller also because the effector of force, i.e., the calibrated coiled-coils, and the fluorescence reporters are physically separated. The self-propagating intermolecular interactions of the coiled-coil force sensors are triggered by transient force on End4p, and the effect of force is amplified both spatially and temporally through the generation of condensates that have micrometer diameters and outlast the lifetime of the endocytic coat. The combination of the small size and the clear readout makes our coiled-coil based strategy a promising tool for *in vivo* force measurements in previously inaccessible locations, and an exciting platform for further development.

We estimate the force on each End4p molecule to be in the 8-10 pN range after the lipid-binding ANTH domain, in the 10-11 pN range between the proline rich domain and the dimerization domain, and in the 11-20 pN range before the THATCH domain (Fig. 4e). Since previous quantitative microscopy studies showed there are up to ~120 End4p molecules per endocytic coat[9], our data suggest that forces in the 1320-2400 pN range are generated by the actin meshwork on End4p at the periphery of the endocytic coat, and at least 960-1200 pN is transmitted directly to the lipid membrane by End4p ANTH domain. These forces on End4p are smaller but in the same order of magnitude as the total endocytosis forces predicted by theory. Total forces on the plasma membrane are likely larger since we showed that force transmission in the endocytic coat is relayed through the binding to other adaptor proteins, as fragments of End4p that do not bind actin are still under tension in the endocytic coat (Fig. 4b, 4c). We speculate that the Sla1p/Pan1p/End3p protein complex, which arrives later than End4p in the assembly of the endocytic coat and has been shown to have interactions with both End4p and Ent1p, bridges the transmission of force from F-actin to End4p (Fig. 4e)[44,45]. The clathrin lattice is probably a hub for integrating the transmission of force in the endocytic coat, as End4p, Ent1p, Sla1p and numerous other endocytic adaptor proteins bind to the clathrin lattice, and we detected a change in the magnitude of force on End4p before and after its dimerization domain, which contains the putative clathrin binding site[19,20]. The heavily interconnected endocytic coat ensures redundancy to robustly transmit forces during CME. We expect the magnitudes of forces during CME to be slightly smaller in budding yeast because turgor pressure there is slightly lower, and we expect the forces to be even smaller in mammalian cells where turgor pressure is several orders of magnitude lower. The redundancy in force transmission through the binding of endocytic coat proteins, however, is probably conserved.

The active involvement of protein phase separation during natural cellular processes is increasingly appreciated. Force produced by the cytoskeleton or motor proteins may change the folding of protein domains to promote or inhibit protein phase separation. The phase separation of LIMD1 recruits focal adhesion proteins in a force dependent manner[46]. The prevalence of low-affinity interactions in the endocytic coat suggests the potential involvement of protein phase separation in normal CME[47–49], which might be more transient in the natural state but seems to be enhanced by the insertion of the coiled-coil force sensors within End4p.

Although we did not focus on the *in vitro* characterization of the phase-separating properties of End4p proteins with coiled-coil insertions, our *in vivo* data offer a clear mechanism for the phase separation of End4p constructs. We show that valency amplification from zero to two following the unfolding of coiled-coils is critical for generating End4p condensates (Fig. 2b, S6g), and that the disconnection of two α-helices, which prevents intermolecular interactions (Fig. 2f), disrupts End4p condensates. Our coiled-coil force sensors therefore represent a new way to induce *in vivo* protein condensates, joining currently existing approaches using light or small molecules. The ample knowledge related to the design and engineering of coiled-coils pave the road for additional functionalities based on this simple protein motif.

Reference

1. Kukulski, W., Schorb, M., Kaksonen, M. & Briggs, J. A. G. Plasma Membrane Reshaping during Endocytosis Is Revealed by Time-Resolved Electron Tomography. *Cell* **150**, 508–520 (2012).
2. Skruzny, M. *et al.* Molecular basis for coupling the plasma membrane to the actin cytoskeleton during clathrin-mediated endocytosis. *Proc. Natl. Acad. Sci. U. S. A.* **109**, E2533–E2542 (2012).
3. Skruzny, M., Pohl, E., Gnoth, S., Malengo, G. & Sourjik, V. The protein architecture of the endocytic coat analyzed by FRET microscopy. *Mol. Syst. Biol.* **16**, e9009 (2020).
4. Legendre-Guillemin, V. ENTH/ANTH proteins and clathrin-mediated membrane budding. *J. Cell Sci.* **117**, 9–18 (2004).
5. Mettlen, M., Chen, P.-H., Srinivasan, S., Danuser, G. & Schmid, S. L. Regulation of Clathrin-Mediated Endocytosis. *Annu. Rev. Biochem.* **87**, 871–896 (2018).
6. Kaksonen, M. & Roux, A. Mechanisms of clathrin-mediated endocytosis. *Nat. Rev. Mol. Cell Biol.* **19**, 313–326 (2018).
7. McMahon, H. T. & Boucrot, E. Molecular mechanism and physiological functions of clathrin-mediated endocytosis. *Nat. Rev. Mol. Cell Biol.* **12**, 517–533 (2011).
8. Mosesson, Y., Mills, G. B. & Yarden, Y. Derailed endocytosis: an emerging feature of cancer. *Nat. Rev. Cancer* **8**, 835–850 (2008).
9. Sun, Y. *et al.* Direct comparison of clathrin-mediated endocytosis in budding and fission yeast reveals conserved and evolvable features. *eLife* **8**, e50749 (2019).
10. Baggett, J. J., D'Aquino, K. E. & Wendland, B. The Sla2p Talin Domain Plays a Role in Endocytosis in Saccharomyces cerevisiae. *Genetics* **165**, 1661–1674 (2003).
11. Maldonado-Báez, L. & Wendland, B. Endocytic adaptors: recruiters, coordinators and regulators. *Trends Cell Biol.* **16**, 505–513 (2006).
12. Skruzny, M. *et al.* An Organized Co-assembly of Clathrin Adaptors Is Essential for Endocytosis. *Dev. Cell* **33**, 150–162 (2015).

13. Lacy, M., Ma, R., Ravindra, N. & letters, B.-J. Molecular mechanisms of force production in clathrin mediated endocytosis. *FEBS Lett.* (2018).
14. Ma, R. & Berro, J. Endocytosis against high turgor pressure is made easier by partial coating and freely rotating base. *Biophys. J.* **120**, 1625–1640 (2021).
15. Basu, R., Munteanu, E. L. & Chang, F. Role of turgor pressure in endocytosis in fission yeast. *Mol. Biol. Cell* **25**, 679–687 (2014).
16. Aghamohammadzadeh, S. & Ayscough, K. R. Differential requirements for actin during yeast and mammalian endocytosis. *Nat. Cell Biol.* **11**, 1039–1042 (2009).
17. Messa, M. *et al.* Epsin deficiency impairs endocytosis by stalling the actin-dependent invagination of endocytic clathrin-coated pits. *eLife* **3**, (2013).
18. Aguilar, R. C., Watson, H. A. & Wendland, B. The Yeast Epsin Ent1 Is Recruited to Membranes through Multiple Independent Interactions. *J. Biol. Chem.* **278**, 10737–10743 (2003).
19. Engqvist-Goldstein, Å. E. Y. *et al.* The actin-binding protein Hip1R associates with clathrin during early stages of endocytosis and promotes clathrin assembly in vitro. *J. Cell Biol.* **154**, 1209–1224 (2001).
20. Wilbur, J. D. *et al.* Actin Binding by Hip1 (Huntingtin-interacting Protein 1) and Hip1R (Hip1-related Protein) Is Regulated by Clathrin Light Chain. *J. Biol. Chem.* **283**, 32870–32879 (2008).
21. Smith, S. M., Baker, M., Halebian, M. & Smith, C. J. Weak Molecular Interactions in Clathrin-Mediated Endocytosis. *Front. Mol. Biosci.* **4**, (2017).
22. Garcia-Alai, M. M. *et al.* Epsin and Sla2 form assemblies through phospholipid interfaces. *Nat. Commun.* **9**, 328 (2018).
23. Zhuo, Y. *et al.* Nuclear Magnetic Resonance Structural Mapping Reveals Promiscuous Interactions between Clathrin-Box Motif Sequences and the N-Terminal Domain of the Clathrin Heavy Chain. *Biochemistry* **54**, 2571–2580 (2015).
24. Miao, Y., Tipakornsaowapak, T., Zheng, L., Mu, Y. & Lewellyn, E. Phospho-regulation of intrinsically disordered proteins for actin assembly and endocytosis. *FEBS J.* **285**, 2762–2784 (2018).

25. Bracha, D., Walls, M. T. & Brangwynne, C. P. Probing and engineering liquid-phase organelles. *Nat. Biotechnol.* **37**, 1435–1445 (2019).

26. Bracha, D. *et al.* Mapping Local and Global Liquid Phase Behavior in Living Cells Using Photo-Oligomerizable Seeds. *Cell* **175**, 1467-1480.e13 (2018).

27. Nakamura, H. *et al.* Intracellular production of hydrogels and synthetic RNA granules by multivalent molecular interactions. *Nat. Mater.* **17**, 79–89 (2018).

28. Tanenbaum, M. E., Gilbert, L. A., Qi, L. S., Weissman, J. S. & Vale, R. D. A protein tagging system for signal amplification in gene expression and fluorescence imaging. *Cell* **159**, 635–646 (2014).

29. Truebestein, L. & Leonard, T. A. Coiled□coils: The long and short of it. *Bioessays* **38**, 903–916 (2016).

30. Lebar, T., Lainšček, D., Merljak, E., Aupič, J. & Jerala, R. A tunable orthogonal coiled-coil interaction toolbox for engineering mammalian cells. *Nat. Chem. Biol.* **16**, 513–519 (2020).

31. Goktas, M. *et al.* Molecular mechanics of coiled coils loaded in the shear geometry. *Chem. Sci.* **9**, 4610–4621 (2018).

32. Gao, Y., Sirinakis, G. & Zhang, Y. Highly Anisotropic Stability and Folding Kinetics of a Single Coiled Coil Protein under Mechanical Tension. *J. Am. Chem. Soc.* **133**, 12749–12757 (2011).

33. Xi, Z., Gao, Y., Sirinakis, G., Guo, H. & Zhang, Y. Single-molecule observation of helix staggering, sliding, and coiled coil misfolding. *Proc. Natl. Acad. Sci.* **109**, 5711–5716 (2012).

34. Pandya, M. J. *et al.* Sticky-End Assembly of a Designed Peptide Fiber Provides Insight into Protein Fibrillogenesis. *Biochemistry* **39**, 8728–8734 (2000).

35. Harbury, P. B., Zhang, T., Kim, P. S. & Alber, T. A switch between two-, three-, and four-stranded coiled coils in GCN4 leucine zipper mutants. *Science* **262**, 1401–1407 (1993).

36. Abella, M., Andruck, L., Malengo, G. & Skruzny, M. Force requirements of endocytic vesicle formation. *bioRxiv* 2020.11.11.378273 (2020) doi:10.1101/2020.11.11.378273.

37. McCann, R. O. & Craig, S. W. The I/LWEQ module: a conserved sequence that signifies F-actin binding in functionally diverse proteins from yeast to mammals. *Proc. Natl. Acad. Sci. U. S. A.* **94**, 5679–5684 (1997).

38. Brett, T. J., Legendre-Guillemin, V., McPherson, P. S. & Fremont, D. H. Structural definition of the F-actin–binding THATCH domain from HIP1R. *Nat. Struct. Mol. Biol.* **13**, 121–130 (2006).

39. O'Shea, E. K., Lumb, K. J. & Kim, P. S. Peptide 'Velcro': Design of a heterodimeric coiled coil. *Curr. Biol.* **3**, 658–667 (1993).

40. Gurnon, D. G., Whitaker, J. A. & Oakley, M. G. Design and Characterization of a Homodimeric Antiparallel Coiled Coil. *J. Am. Chem. Soc.* **125**, 7518–7519 (2003).

41. Moll, J. R., Ruvinov, S. B., Pastan, I. & Vinson, C. Designed heterodimerizing leucine zippers with a ranger of pIs and stabilities up to 10−15 M. *Protein Sci. Publ. Protein Soc.* **10**, 649–655 (2001).

42. Dmitrieff, S. & Nédélec, F. Membrane Mechanics of Endocytosis in Cells with Turgor. *PLOS Comput. Biol.* **11**, (2015).

43. Nickaeen, M., Berro, J., Pollard, T. D. & Slepchenko, B. M. Simulation of the mechanics of actin assembly during endocytosis in yeast. *bioRxiv* 518423 (2019) doi:10.1101/518423.

44. Sun, Y., Leong, N., Wong, T. & Drubin, D. A Pan1/End3/Sla1 complex links Arp2/3-mediated actin assembly to sites of clathrin-mediated endocytosis. *Mol. Biol. Cell* **26**, 3841–3856 (2015).

45. Tang, H.-Y., Xu, J. & Cai, M. Pan1p, End3p, and Sla1p, Three Yeast Proteins Required for Normal Cortical Actin Cytoskeleton Organization, Associate with Each Other and Play Essential Roles in Cell Wall Morphogenesis. *Mol. Cell. Biol.* **20**, 12–25 (2000).

46. Wang, Y. *et al.* LIMD1 phase separation contributes to cellular mechanics and durotaxis by regulating focal adhesion dynamics in response to force. *Dev. Cell* **56**, 1313-1325.e7 (2021).

47. Kozak, M. & Kaksonen, M. *Phase separation of Ede1 promotes the initiation of endocytic events*. http://biorxiv.org/lookup/doi/10.1101/861203 (2019) doi:10.1101/861203.

48. Day, K. J. *et al.* Liquid-like protein interactions catalyse assembly of endocytic vesicles. *Nat. Cell Biol.* **23**, 366–376 (2021).

49. Bergeron-Sandoval, L.-P. *et al.* Proteins with prion-like domains can form viscoelastic condensates that enable membrane remodeling and endocytosis. *bioRxiv* 145664 (2021) doi:10.1101/145664.

50. Fernandez, R. & Berro, J. Use of a fluoride channel as a new selection marker for fission yeast plasmids and application to fast genome editing with CRISPR/Cas9. *Yeast Chichester Engl.* **33**, 549–557 (2016).

Materials and methods

Protein constructs and purification

The codon optimized DNA of coiled-coils were synthesized (Invitrogen) and cloned into pGEX-6P-1 vectors (Sigma-Aldrich) after PCR amplification and Gibson cloning (New England BioLabs). Constructs were confirmed by DNA sequencing and introduced into BL21 (DE3) (New England BioLabs) for protein expression. GST fusion proteins were purified by binding to Glutathione Sepharose 4B beads (GE Healthcare) and the GST tag was removed by cleaving with PreScission Protease (Sigma-Aldrich). The purified proteins were exchanged to the biotinylation buffer containing 25 mM HEPES, 200 mM potassium glutamate with pH 7.7 and biotinylated at the Avi-tag in the presence of 50 μg/mL BirA, 50 mM bicine buffer, pH 8.3, 10 mM ATP, 10 mM magnesium acetate, and 50 μM d-biotin (Avidity) at 4°C overnight.

Protein-DNA handle crosslinking

The PCR-generated DNA handle used in the single-molecule experiments was 2,260 bp in length and contained a thiol group (-SH) at one end and two digoxigenin moieties at the other end. The DNA handle was crosslinked to the coiled coil protein construct as was described previously[32]. Briefly, the protein construct was mixed with the DTDP-treated DNA handle in a 50:1 molar ratio in 100 mM phosphate buffer, 500 mM NaCl, pH 8.5 and incubated at room temperature overnight.

Single-molecule manipulation experiments

All pulling experiments were performed using dual-trap high-resolution optical tweezers as previously described[32,33]. Briefly, an aliquot of the crosslinked protein-DNA mixture was mixed with 5 μL 2.1 μm diameter anti-digoxigenin antibody coated polystyrene beads (Spherotech) and incubated at room temperature for 15 min. Then the anti-digoxigenin coated beads and 0.5 μL 1.7 μm diameter streptavidin-coated beads were diluted in 1 mL PBS buffer (137 mM NaCl, 2.7 mM KCl, 8.1 mM Na_2HPO_4, 1.8 mM KH_2PO_4, pH 7.4) and were separately injected into the top and bottom channels of a homemade microfluidic chamber. Both channels were connected to the central channel with glass tubing. The two beads entering the central channel were caught in two optical traps and brought close to allow a single protein to be tethered between them. All manipulation experiments were carried out in the PBS buffer supplemented with the oxygen scavenging system (400 mg/mL glucose (Sigma-Aldrich), 0.02 unit/mL glucose oxidase (Sigma-Aldrich), and 0.06 unit/mL catalase). All single molecules were pulled and relaxed by increasing and decreasing, respectively, the trap separation at a speed of 10 nm/s. The data was processed by MATLAB codes as were described elsewhere[32,33] and the unfolding forces were determined from the force-extension curves.

Yeast strains and media

The *S. pombe* strains used in this study are presented in Supplemental Table S1. Strains were constructed using the method described in our previous publication[50], and verified by sequencing of the colony PCR products. Fission yeast cells were grown in YE5S (Yeast Extract supplemented with 0.225 g/L of uracil, lysine, histidine, adenine and leucine), and imaged in

EMM5S (Edinburgh Minimum media supplemented with 0.225 g/L of uracil, lysine, histidine, adenine and leucine). Yeast cells were grown at 32 °C under 200 rpm shaking overnight to reach exponential phase at OD_{595nm} between 0.3 and 0.5.

Microscopy

Cells were imaged on 25% gelatin pad at room temperature on a Nikon TiE inverted microscope (Nikon, Tokyo, Japan) with a CSU-W1 Confocal Scanning Unit (Yokogawa Electric Corporation, Tokyo, Japan) under a CFI Plan Apo 100X/1.45NA Phase objective (Nikon, Tokyo, Japan). Images were acquired with an iXon Ultra888 EMCCD camera (Andor, Belfast, UK). mEGFP tagged strains were excited with a 488-nm argon-ion laser and filtered by Spectra X with a single band pass filter 510/25. mScarlet-I tagged strains were excited with a 561-nm argon-ion laser and filtered by Spectra X with a single band pass filter 575/25. Fluorescent signals from the whole cell were collected with 21 optical sections separated by 0.5 µm, and max projected to create 2D images. The laser excitation and image acquisition settings for the same fluorophore (mEGFP or mScarlet-I) were the same for all strains imaged. Images were displayed and analyzed with the Fiji distribution of ImageJ (NIH, USA).

LatA treatment

Cells were washed with EMM5S and loaded into CellASIC microfluidics chambers (Y04C-02-5PK, Millipore-Sigma, Saint Louis, USA) before LatA (Thermo Fisher, MA, USA) treatment. The media exchange was controlled by the CellASIC ONIX2 microfluidics system (Millipore-Sigma, Saint Louis, USA) with a flow pressure of 4 psi. LatA was diluted in EMM5S to a final concentration of 100 µM. Fluorescent signals from the whole cell were collected with 21 optical sections each with 0.5 µm thickness, and stacks were projected with average intensity. Cells were imaged every 5 minutes, and the final images were corrected for photobleaching (exponential fit) before being analyzed.

Protein condensate analysis

For the quantification of End4p protein condensates, we created an ImageJ plugin that identifies protein condensates and excludes End4p patches based on fluorescence intensity (900-65535), size (4-500 pixel) and circularity (0.2-1.0). Our plugin shows good agreement with manual selection. Examples of automatically identified protein condensates are shown in Figure S4.

Acknowledgements:

We thank the Yale West Campus Imaging Core for providing access to the spinning disc confocal microscope. We thank Xiaolei Su, Martin Schwartz, Min Wu, Valentina Greco, Daniel Suter, Yue Liu, Mathis Riehle, Jim Rothman and Tom Pollard for their comments on the manuscript. This research was supported by National Institutes of Health/National Institute of General Medical Sciences Grant R21GM132661 to J. B. and R35GM131714 to Y. Z.

Table S1. *S. pombe* strains used in this study.

Strain	Genotype	Reference
JB367	end4-mEGFP fex1Δ fex2Δ ade6-M216 his3-D1 leu1-32 ura4-D18 h-	This study
JB561	mScarlet-I-end4-mEGFP fex1Δ fex2Δ ade6-M216 his3-D1 leu1-32 ura4-D18 h-	This study
JB562	mScarlet-I-end4 fex1Δ fex2Δ ade6-M216 his3-D1 leu1-32 ura4-D18 h-	This study
JB577	mScarlet-I-end4-ERBV-1-20AA-end4-mEGFP fex1Δ fex2Δ ade6-M216 his3-D1 leu1-32 ura4-D18 h-	This study
JB586	mScarlet-I-end4ΔC fex1Δ fex2Δ ade6-M216 his3-D1 leu1-32 ura4-D18 h-	This study
JB592	mScarlet-I-end4-GCN4-pIL-I16N-5E3R-2A-GCN4-pIL-I16N-5R3E-end4-mEGFP fex1Δ fex2Δ ade6-M216 his3-D1 leu1-32 ura4-D18 h-	This study
JB597	mScarlet-I-end4-GCN4-pIL-I16N-5E3R-2A-MUT-GCN4-pIL-I16N-5R3E-end4-mEGFP fex1Δ fex2Δ ade6-M216 his3-D1 leu1-32 ura4-D18 h-	This study
JB617	mScarlet-I-end4-Oakley-p1-OnePlus-end4-mEGFP fex1Δ fex2Δ ade6-M216 his3-D1 leu1-32 ura4-D18 h-	This study
JB619	mScarlet-I-end4-GCN4-pIL-I16N-5E3R-10G-GCN4-pIL-I16N-5R3E-end4-mEGFP fex1Δ fex2Δ ade6-M216 his3-D1 leu1-32 ura4-D18 h-	This study
JB643	end4-Velcro-p1-end4-mEGFP fex1Δ fex2Δ ade6-M216 his3-D1 leu1-32 ura4-D18 h-	This study
JB675	mScarlet-I-end4-GCN4-pIL-I16N-5E3R-2A_Mut-pIL-I16N-5R3E fex1Δ fex2Δ ade6-M216 his3-D1 leu1-32 ura4-D18 h-	This study
JB689	mScarlet-I-end4-ERBV1-20AA-GCN4-pIL-I16N-5E3R-2A_Mut-GCN4-pIL-I16N-5R3E-end4-mEGFP fex1Δ fex2Δ ade6-M216 his3-D1 leu1-32 ura4-D18 h-	This study
JB691	mScarlet-I-end4-ANTH-GCN4-pIL-I16N-5E3R-2A_Mut-GCN4-pIL-I16N-5R3E-end4-mEGFP fex1Δ fex2Δ ade6-M216 his3-D1 leu1-32 ura4-D18 h-	This study
JB693	mScarlet-I-end4-ANTH-Pro-ERBV1-20AA-end4-mEGFP fex1Δ fex2Δ ade6-M216 his3-D1 leu1-32 ura4-D18 h-	This study
JB694	mScarlet-I-end4-ANTH-Pro-GCN4-pIL-I16N-5E3R-2A_Mut-GCN4-pIL-I16N-5R3E-end4-mEGFP fex1Δ fex2Δ ade6-M216 his3-D1 leu1-32 ura4-D18 h-	This study
JB717	mScarlet-I-end4-pER-E-GGGS-pER-R-end4-mEGFP fex1Δ fex2Δ ade6-M216 his3-D1 leu1-32 ura4-D18 h-	This study
JB726	mScarlet-I-end4-1010DDD-mEGFP fex1Δ fex2Δ ade6-M216 his3-D1 leu1-32 ura4-D18 h-	This study
JB727	mScarlet-I-end4-V856-GCN4-pIL-I16N-5E3R-2A_Mut-GCN4-pIL-I16N-5R3E-1010DDD-mEGFP fex1Δ fex2Δ ade6-M216 his3-D1 leu1-32 ura4-D18 h-	This study
JB728	mScarlet-I-end4-R1093G-mEGFP fex1Δ fex2Δ ade6-M216 his3-D1 leu1-32 ura4-D18 h-	This study
JB729	mScarlet-I-end4-V856-GCN4-pIL-I16N-5E3R-2A_Mut-GCN4-pIL-	This study

	I16N-5R3E-R1093G-mEGFP fex1Δ fex2Δ ade6-M216 his3-D1 leu1-32 ura4-D18 h-	
JB730	mScarlet-I-end4-GCN4-pIL-I16N-5E3R-2A_Mut-GCN4-pIL-5R3E-ΔC fex1Δ fex2Δ ade6-M216 his3-D1 leu1-32 ura4-D18 h-	This study
JB735	mScarlet-I-end4-pER-E-10G-pER-R-end4-mEGFP fex1Δ fex2Δ ade6-M216 his3-D1 leu1-32 ura4-D18 h-	This study
JB736	mScarlet-I-end4-ANTH-Pro-ERBV1-20AA-V856-GCN4-pIL-I16N-5E3R-2A_Mut-GCN4-pIL-I16N-5R3E-end4-mEGFP fex1Δ fex2Δ ade6-M216 his3-D1 leu1-32 ura4-D18 h-	This study
JB743	mScarlet-I-end4-ANTH-Pro-Velcro-p1-end4-mEGFP fex1Δ fex2Δ ade6-M216 his3-D1 leu1-32 ura4-D18 h-	This study
JB753	mScarlet-I-end4-ANTH-Pro-Velcro-p1-end4-R1093G-mEGFP fex1Δ fex2Δ ade6-M216 his3-D1 leu1-32 ura4-D18 h-	This study
JB760	mScarlet-I-end4-ANTH-Velcro-p1-end4-mEGFP fex1Δ fex2Δ ade6-M216 his3-D1 leu1-32 ura4-D18 h-	This study
JB762	mScarlet-I-end4-ANTH-Pro-Oakley-p1-OnePlus-end4-mEGFP fex1Δ fex2Δ ade6-M216 his3-D1 leu1-32 ura4-D18 h-	This study
JB767	mScarlet-I-end4-ANTH-Oakley-p1-OnePlus-end4-mEGFP fex1Δ fex2Δ ade6-M216 his3-D1 leu1-32 ura4-D18 h-	This study
JB772	mScarlet-I-end4-ANTH-pER-E-GGGS-pER-R-end4-mEGFP fex1Δ fex2Δ ade6-M216 his3-D1 leu1-32 ura4-D18 h-	This study
JB773	mScarlet-I-end4-ANTH-Pro-pER-E-GGGS-pER-R-end4-mEGFP fex1Δ fex2Δ ade6-M216 his3-D1 leu1-32 ura4-D18 h-	This study
JB780	mScarlet-I-end4-ANTH-Velcro-p1-R1093G-end4-mEGFP fex1Δ fex2Δ ade6-M216 his3-D1 leu1-32 ura4-D18 h-	This study
JB798	mScarlet-I-end4-Oakley-p1-OnePlus-R1093G-end4-mEGFP fex1Δ fex2Δ ade6-M216 his3-D1 leu1-32 ura4-D18 h-	This study
JB799	mScarlet-I-end4-Velcro-p1-R1093G-end4-mEGFP fex1Δ fex2Δ ade6-M216 his3-D1 leu1-32 ura4-D18 h-	This study
JB800	mScarlet-I-end4-pER-E-GGGS-pER-R-R1093G-end4-mEGFP fex1Δ fex2Δ ade6-M216 his3-D1 leu1-32 ura4-D18 h-	This study

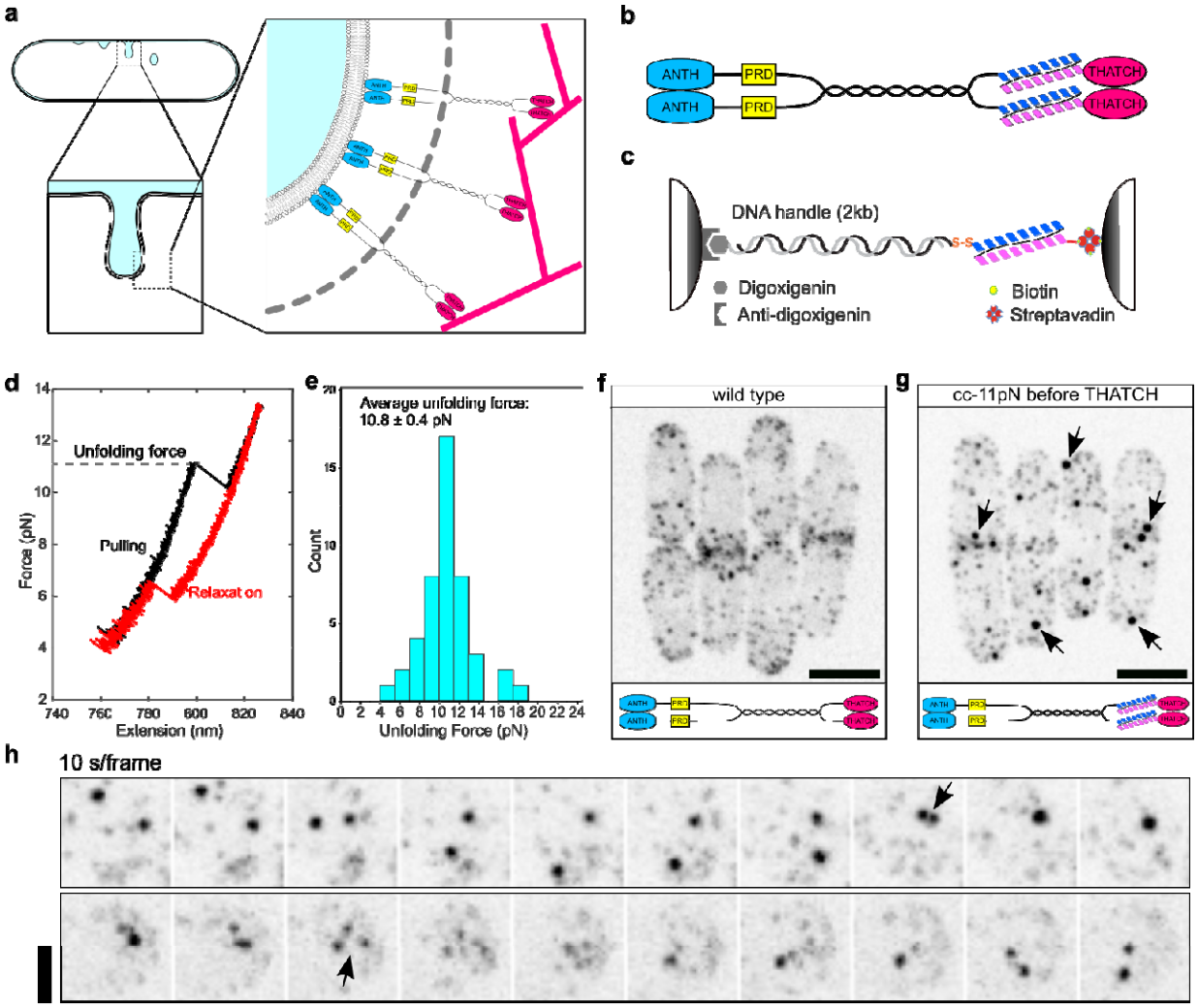

Figure 1. Insertion of a calibrated coiled-coil force sensor within End4p leads to the formation of End4p condensates. a, End4p links the lipid membrane to F-actin at sites of clathrin-mediated endocytosis. Upper left, cross section of a fission yeast cell with endocytic pits at different stages. Lower left, side view of an endocytic pit with invaginated membrane. Right, End4p dimers traverses the clathrin coat (gray dotted curve) to transmit the forces generated by the assembly of actin filaments (magenta rods) to deform the plasma membrane. Cyan: End4p lipid binding **A**P180 **N**-**T**erminal **H**omology (ANTH) domain; yellow: End4p proline rich domain; magenta: End4p F-actin binding **t**alin-**H**IP1/R/Sla2p **a**ctin-**t**ethering **C**-terminal **h**omology (THATCH) domain. Drawings are not to scale. **b**, Schematic of an End4p dimer with the insertion of the coiled-coil force sensor before the THATCH domain. **c**, Schematic of the constructs used to calibrate the coiled-coil force sensor with optical tweezers. The coiled-coil is attached to two beads trapped by optical tweezers through a 2260-bp DNA handle. **d**, Representative force-extension curves obtained by pulling (back curve) and then relaxing (red curve) the coiled-coil force sensor. **e**, Distribution of the unfolding force for the coiled-coil force sensor cc-11pN (N=46). The average unfolding force is presented as mean ± SEM. **f**, representative fission yeast cells expressing fluorescently-tagged wild-type End4p. End4p is

mostly found in endocytic patches that are enriched at cell tips and the division plane. See also Fig. S1 and movie 1. **g**, Representative fission yeast cells expressing fluorescently-tagged End4p with cc-11pN inserted before the THATCH domain as in **b**. Multiple large persistent spherical condensates of End4p constructs (indicated by arrows) can be distinguished from transient diffraction limited endocytic patches. **h**, End4p condensates display liquid-like behaviors. Upper panel, fusion of two End4p condensates (arrow). Lower panel, fission of one End4p condensate into two smaller condensates (arrow). See the full dynamics of End4p condensates in Fig. S2, movie 2 and movie 3. **f** and **g**, scale bars: 5 μm. **h**, scale bars: 2 μm. The schematic under each image indicates the modifications on End4p, and fluorescent tags are omitted for clarity.

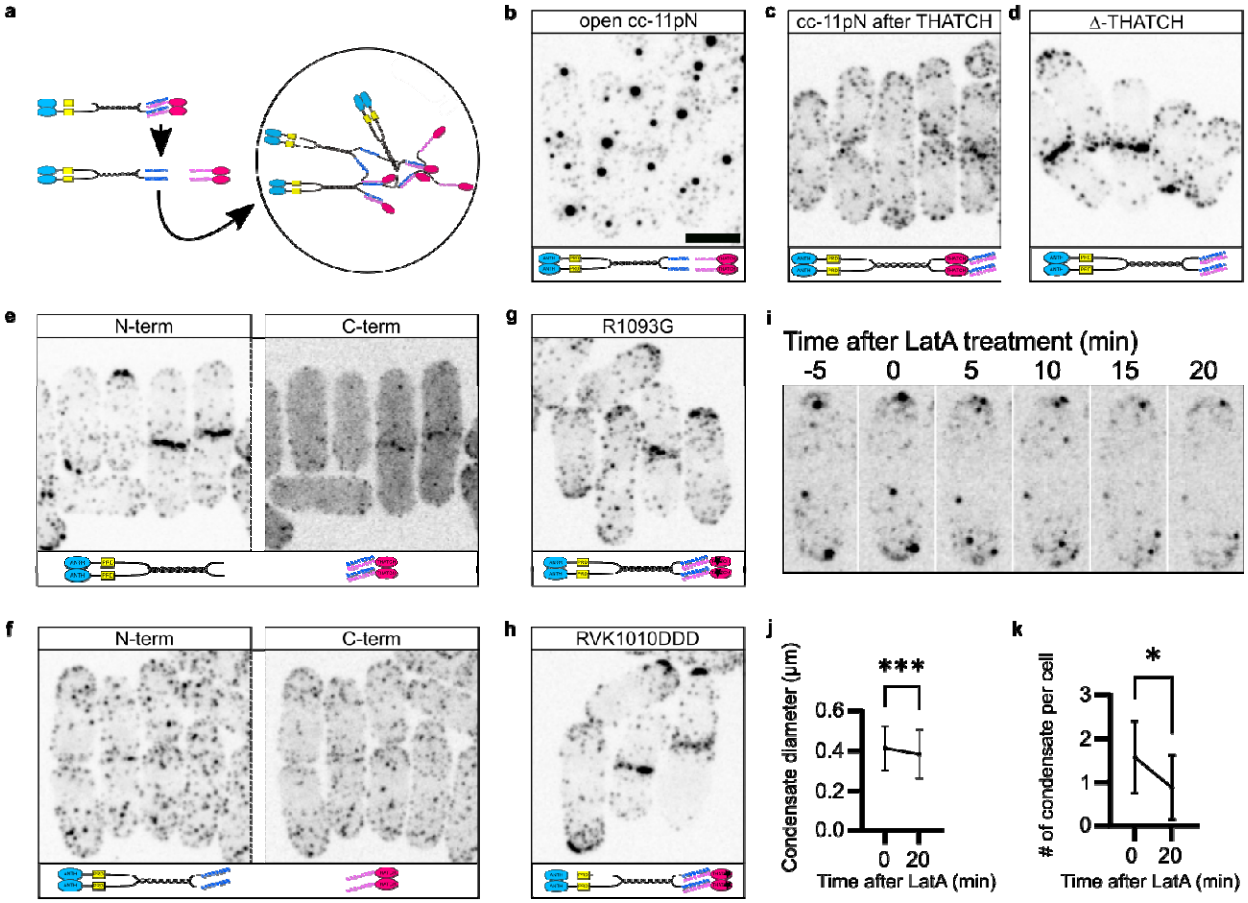

Figure 2. Force-induced unfolding of the coiled-coil force sensor promotes the formation of End4p condensates. a, Schematic of End4p condensate formation. The coiled-coil force sensor unfolds when the magnitude of force on End4p exceeds the unfolding force threshold of the coiled-coil force sensor. During the refolding process of the coiled-coil force sensor, α-helices from different End4p molecules mediate the entanglement of End4p molecules into condensates. See also Fig. S3**e**. **b-i**, Localization of different End4p constructs in fission yeast cells. Both the N- and C-terminal End4p fragments are fluorescently labeled in **e-f**. **b**, The insertion of an open conformation cc-11pN into End4p led to larger End4p condensates. See also Fig. S3**c-d**. **c-e**, The insertion of cc-11pN into End4p does not lead to condensate formation at the absence of force. The force on cc-11pN was removed by inserting after the THATCH domain (**c**), deleting the THATCH domain (**d**), or disconnecting the THATCH domain with the rest of End4p (**e**). **f**, The formation of End4p condensates is dependent on the connection between the two α-helices of cc-11pN. The cleaving of the linker of cc-11pN prevented the formation of condensates. See also Fig. S3**e-f. g-h**, End4p does not form condensates when a cc-11pN was inserted before the THATCH domain, and RVK1010DDD (**g**) or R1093G (**h**) mutations were introduced into the THATCH domain to abolish its binding to F-actin. **i**, Snapshots of fission yeast cells with End4p condensates before and after the treatment with 100 μM LatA. The size (**j**) and number (**k**) of End4p condensates decreases after actin assembly is impaired by the latA treatment. Data in **j-k** are presented as the mean ± SD (>300 condensates from n = 3 independent repeats). Asterisk

indicates a significant difference. **j**, P =0.0003, two-tailed t test. **k**, P =0.01, two-tailed t test. **b-h**, Scale bar in **b** applies to all images, 5 μm. End4p is tagged at the C-terminal with mEGFP in **b-i**, and End4p is also tagged at the N-terminal with mScarlet-I in **e-f**. *In vivo* protein cleaving in **e-f** was achieved by the insertion of a 2A peptide. The schematic under each image indicates the modifications on End4p, and fluorescent tags are omitted for clarity. See the localization of End4p without cc-11pN in Figure S4.

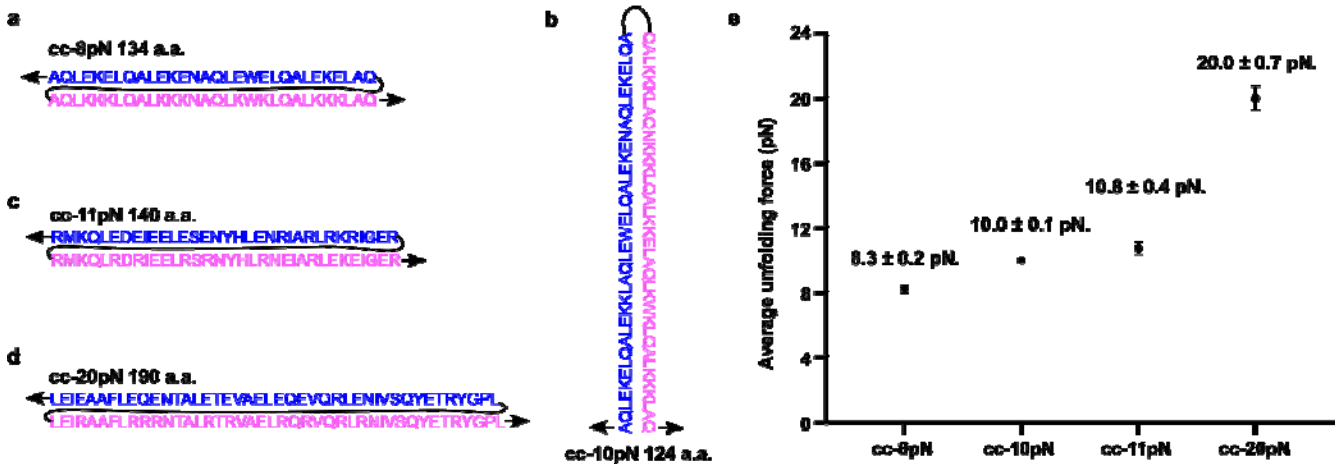

Figure 3. Library of calibrated coiled-coil force sensors. a-d, Sequence and pulling direction (indicated by black arrows) of the coiled-coil force sensors. Among the four force sensors, cc-8pN, cc-11pN and cc-20pN (**a**, **c**, and **d**, respectively) are parallel coiled-coils while cc-10pN (**b**) is an anti-parallel coiled-coil. The flexible linker between the two α-helices (blue and magenta) are drawn as black lines. **e,** Average unfolding forces of the coiled-coil force sensors, presented as mean ± SEM. N=29 for cc-8pN. N=45 for cc-10pN. N=48 for cc-20pN. See the distribution of unfolding forces and controls of the force sensors in Figure S5.

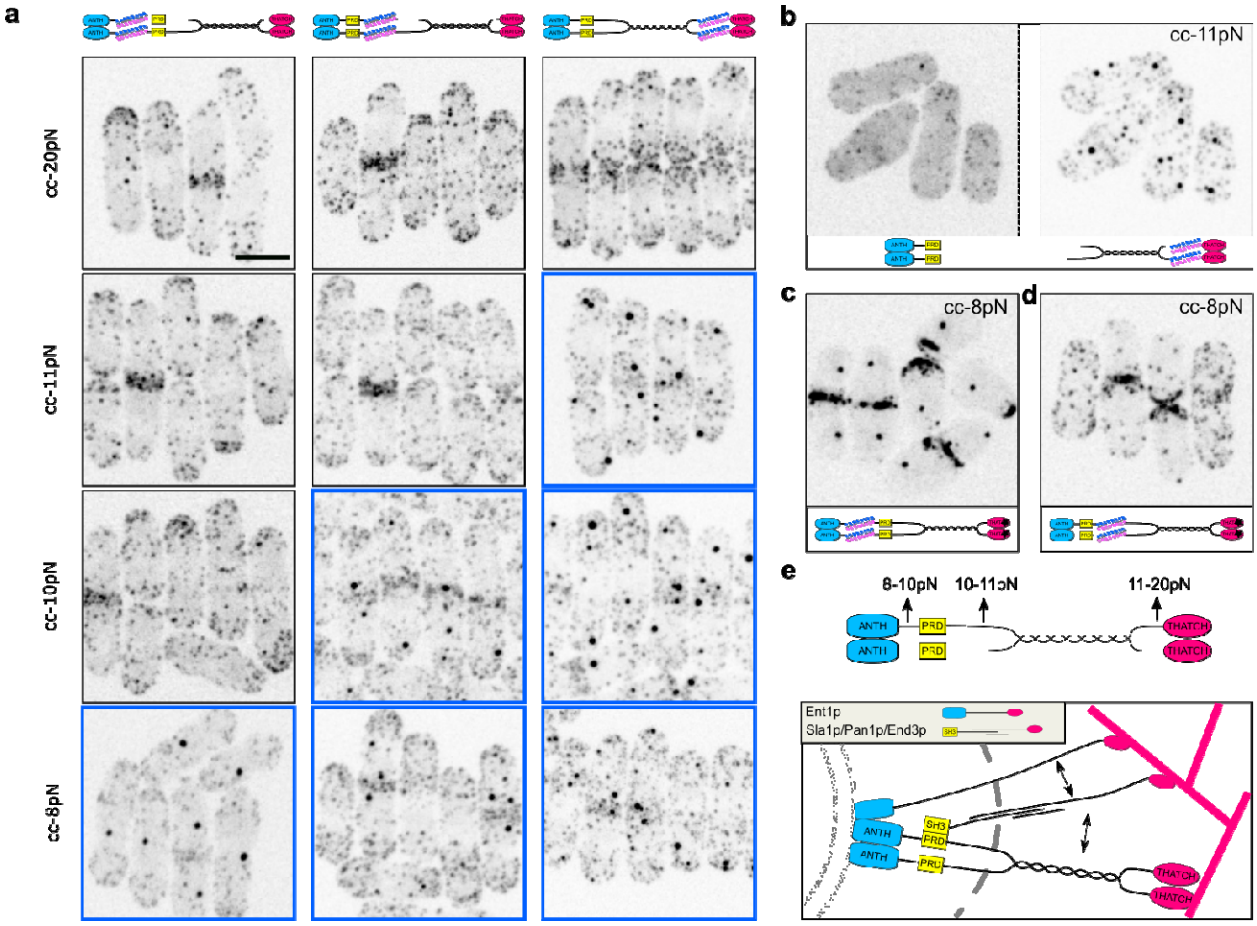

Figure 4. End4p is under a force gradient. a, End4p localization when a calibrated coiled-coil force sensor was inserted after the ANTH domain (first column), after the proline rich domain (second column), or before the THATCH domain (third column). Coiled-coils unfolding thresholds are 20 pN (first row), 11 pN (second row), 10 pN (third row), 8 pN (fourth row). Images containing End4p condensates are boxed in blue frames. **b**, End4p N- and C-terminal localization when a cc-11pN was inserted before the THATCH domain, and a self-cleaving 2A peptide was introduced after the proline rich domain. The End4p C-terminal fragment formed condensates despite its disconnection from the lipid-binding ANTH domain, demonstrating that at least 11 pN of force is transmitted by End4p C-terminal (after the proline-rich domain) to other components of the endocytic machinery. See the localization of End4p fragments without cc-11pN in Figure S3**c**. **c**, End4p localization when a cc-8pN was inserted after the ANTH domain, and an R1093G mutation was introduced into the THATCH domain to abolish its binding to actin filaments. This End4p construct formed condensates despite its inability to bind actin, demonstrating that at least 8 pN of force is transmitted by other components of the endocytic machinery to End4p N-terminal. **d**, End4p localization when a cc-8pN was inserted after the proline rich domain, and an R1093G mutation was introduced into the THATCH domain to abolish its binding to F-actin. This construct didn't form condensates. This result and the result of panel **c** demonstrate that most of the force not transmitted through the THATCH

domain is transmitted through the proline rich domain. **e**, Model of force transmission during CME. Top: distribution of forces on End4p. Our new coiled-coil library allowed us to determine that the forces between different domain of End4p are different. Bottom: hypothetical organization of adaptor proteins across the clathrin coat. End4p and Ent1p make direct interactions with the plasma membrane, the clathrin lattice and actin filaments, and are known mechanical linkers to transmit the forces produced by the actin meshwork to deform the membrane. Other endocytic proteins or protein complexes, through their binding to domains in End4p or Ent1p, also relay force from F-actin to the membrane. Double arrows indicate known protein-protein interactions. Drawings are not to scale. **a-d**, Scale bar in **a** applies to all images, 5 μm. End4p is tagged at the C-terminal with mEGFP in **a-d**, and End4p is also tagged at the N-terminal with mScarlet-I in **b**. The schematic under each image indicates the modifications on End4p, and fluorescent tags are omitted for clarity.

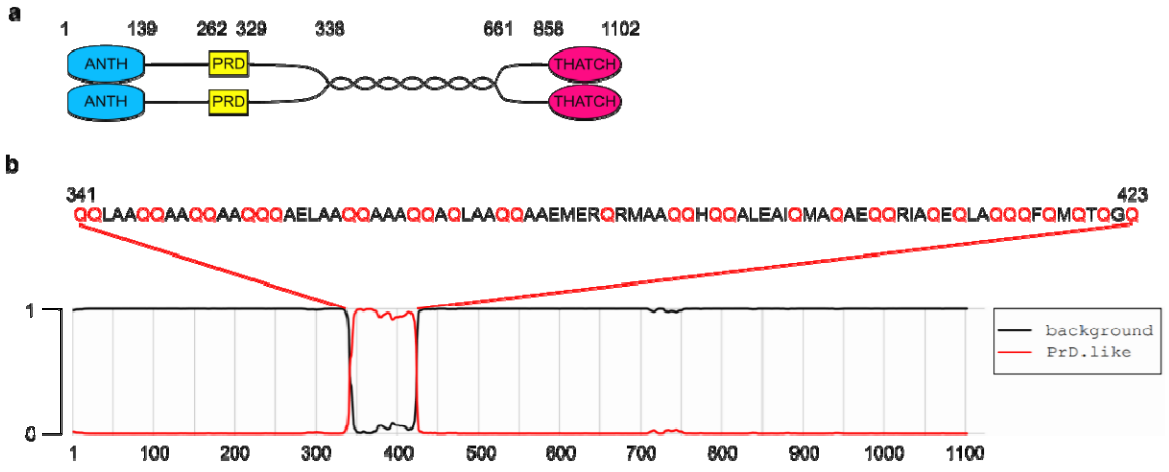

Figure S1. Domain organization of End4p. a, Schematic of End4p dimer. The numbers indicate the residues where domains start and end. The coiled-coil force sensors are inserted after D155, P337, or V856. Drawings are not to scale. **b**, The beginning of End4p dimerization coiled-coil contains a poly-Q region that is predicted to be prion like by Prion Like Amino Acid Composition (PLAAC)[1]. Glutamines (Q) are highlighted in red.

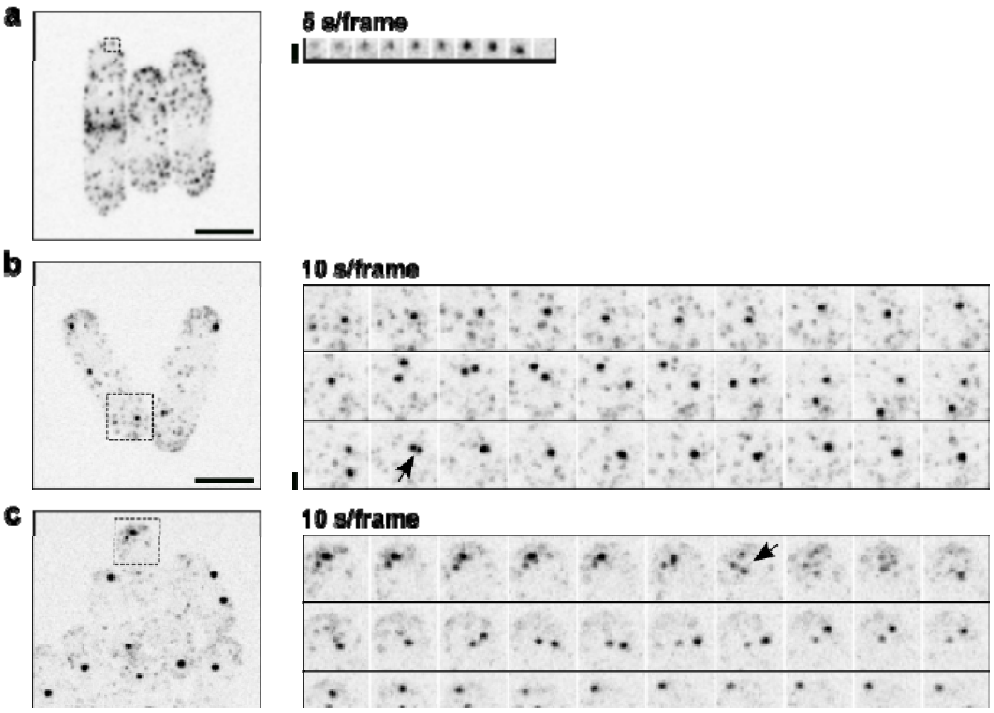

Figure S2. End4p constructs in condensates have longer lifetime than End4p in endocytic sites. a, Representative fission yeast cells with fluorescently tagged wild-type End4p. Right: temporal evolution of End4p in the boxed region. A typical End4p patch lasts less than 50 seconds. See also movie 1. **b-c**, Representative fission yeast cells with fluorescently-tagged End4p where a cc-11pN was inserted before the THATCH domain. Right: temporal evolution of End4p construct in the boxed regions. End4p condensates experience rapid movements across the cell and occasionally fuse with each other (**b**) or split (**c**) (arrows). A subset of this montage is shown in Fig. 1**g**. See also movie 2 (**b**) and movie 3 (**c**). **a-c**, scale bars in the left panels, 5 µm. Scale bars in the right panels, 2 µm. End4p is tagged at the C-terminal with mEGFP in **a-c**. Images are inverted contrast of max projected whole cell sections. Note that the contrast is enhanced in **a** to better visualize a single endocytic event.

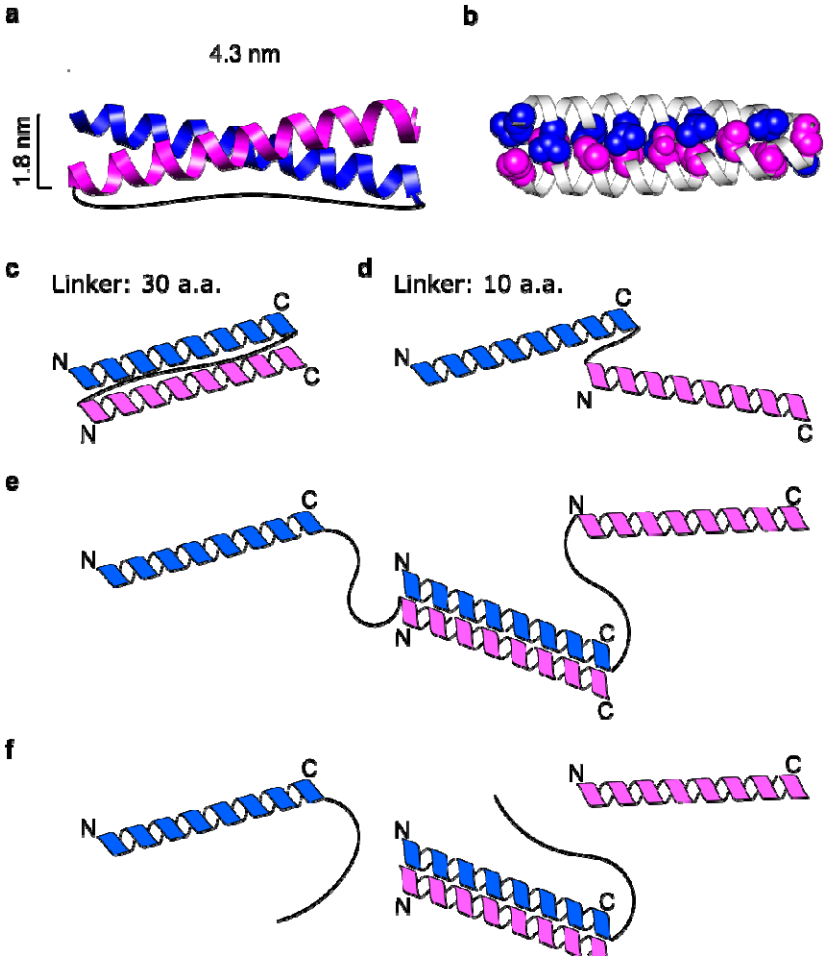

Figure S3. Schematic of coiled-coil force sensors in different conformations. a, Ribbon diagram of cc-11pN in the folded state. The two α-helices (blue and magenta) are connected with a 30-amino acid linker (black line). Dimensions of the coiled-coil are indicated according to the structure of PDB entry 2zta. **b**, The structure of a folded cc-11pN with the residues in the hydrophobic core highlighted. These hydrophobic residues will be exposed when the coiled-coil unfolds under sufficiently large force. **c**, cc-11pN with a 30-amino acid linker folds properly by forming a parallel coiled-coil. **d**, cc-11pN with a 10-amino acid is unable to form a parallel coiled-coil and adopts an open conformation. This open conformation promotes the formation of protein condensates as shown in Fig. 2**a**-**b** and Fig. S4**h**. **e**, An intermolecular connection between two open cc-11pN is formed during the refolding process. Each intermolecular connection generates two exposed α-helices that could mediate further intermolecular connections. **f**, Cleavage at the linker of the two α-helices of cc-11pN prevents the formation of intermolecular connections. See also Fig. 2**f**. The N- and C-terminals of α-helices in **c**-**f** are labeled for orientation.

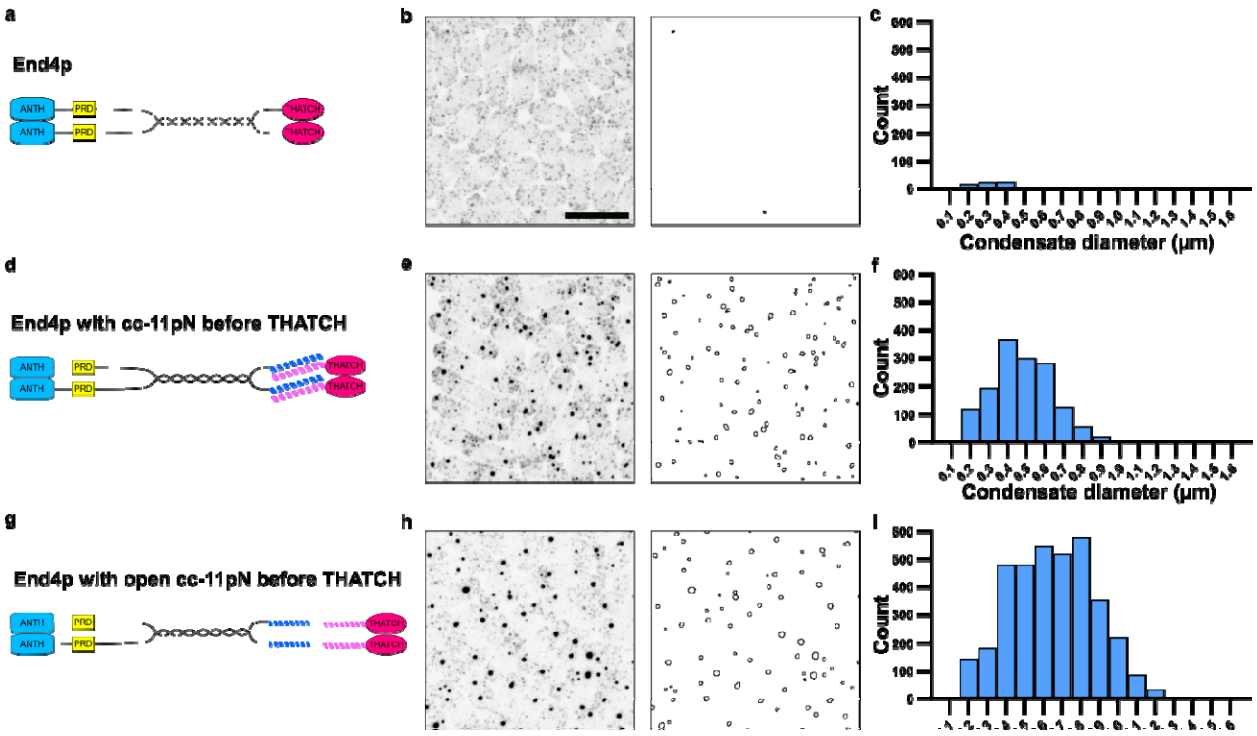

Figure S4. Quantification of protein condensates. End4p condensates have different geometrical properties than End4p patches as analyzed by a custom ImageJ plugin. **a-c,** End4p was tagged at the N-terminal with mEGFP. **d-f,** End4p was tagged at the N-terminal with mEGFP, and a cc-11pN was inserted before the THATCH domain. **g-i,** End4p was tagged at the N-terminal with mEGFP, and a cc-11pN in the open conformation was inserted before the THATCH domain. **b, e, h,** Representative images of fission yeast cells with fluorescently tagged End4p or End4p constructs are shown on the left, and the identified End4p condensates are shown on the right. The distributions of condensate diameter are shown in **c, f, i**, each from >500 cells. A negligible population of End4p patches, typically from spatially overlapping endocytic events, is misidentified as End4p condensates. Scale bar in **b** applies to all images, 10 μm. Images in **b, e, h** are acquired and displayed with the same settings.

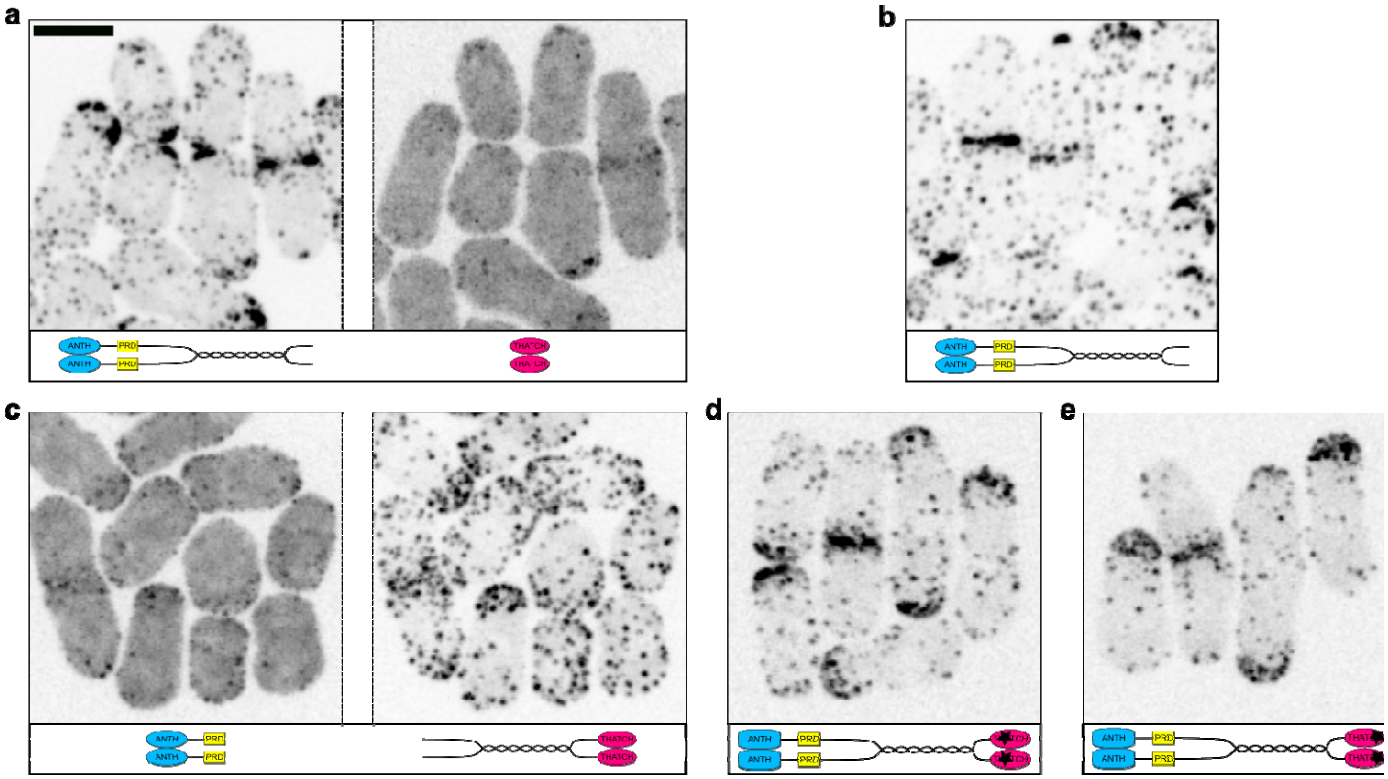

Figure S5. Controls for End4p localization in mutant strains. a, Representative fission yeast cells expressing End4p where a self-cleaving 2A peptide was inserted before the THATCH domain and fluorescently-tagged at its N- and C-terminals. The End4p N-terminal abnormally accumulates at cell tips and the division plane, while End4p C-terminal is diffusive in the cytoplasm. The localization of End4p fragments were not changed by the insertion of cc-11pN as shown in Figure 2**e**. **b**, Representative fission yeast cells expressing fluorescently-tagged End4p where the THATCH domain was deleted. End4p without the THATCH domain abnormally accumulates at cell tips and the division plane. The localization of this End4p construct was not changed by the insertion of cc-11pN as shown in Figure 2**d**. **c**, Representative fission yeast cells expressing fluorescently-tagged End4p where a self-cleaving 2A peptide was inserted after the proline rich domain. End4p N-terminal is diffusive in the cytoplasm, while its C-terminal localizes to endocytic patches. **d**, Representative fission yeast cells expressing fluorescently-tagged End4p where the RVK1010DDD mutation was introduced into the THATCH domain to abolish binding to actin filaments. This mutant abnormally accumulates at cell tips and the division plane. **e**, Representative fission yeast cells expressing fluorescently-tagged End4p where the R1093G mutation was introduced into the THATCH domain to abolish binding to actin filaments. This mutant abnormally accumulates at cell tips and the division plane. The localization of End4p in **d** and **e** were not changed by the insertion of cc-11pN as shown in Figure 2**g** and 2**h**. **a-e**, Scale bar in **a** applies to all images, 5 µm. Images are inverted contrast of max projected whole cell sections. End4p is tagged at the N-terminal with mScarlet-I in **a-e**, and End4p is also tagged at the C-terminal with mEGFP in **a, c, d** and **e**. The schematic under each image indicates the modifications on End4p, and fluorescent tags are omitted for clarity.

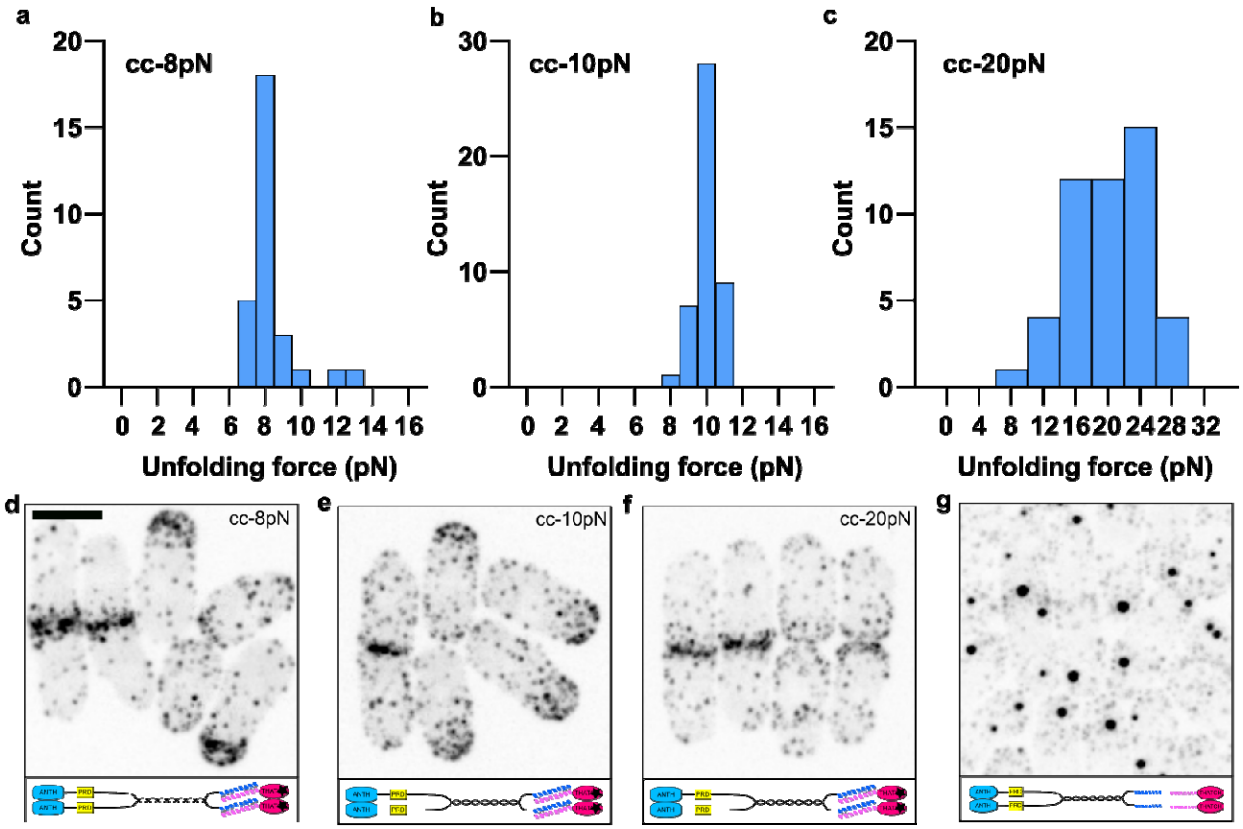

Figure S6. Coiled-coils with different average unfolding forces. a-c, Distribution of the unfolding force for cc-8pN, cc-10pN and cc-20pN. Data are used to calculate the average unfolding force as shown in Figure 3**e**. **d-f**, Representative fission yeast cells expressing fluorescently-tagged End4p where cc-8 pN, cc-10 pN or cc-20 pN was inserted before the THATCH domain, and an R1093G mutation was introduced into the THATCH domain to abolish its binding to actin filaments. End4p shows abnormal accumulation at cell tips and the division plane, without forming condensates. **g**. Representative fission yeast cells expressing fluorescently-tagged End4p where a variant of cc-20pN that is always in an open conformation was inserted before the THATCH domain. The insertion of this "always-open" coiled-coil into End4p led to End4p condensates. **d-g**, Scale bar in **d** applies to all images, 5 µm. Images are inverted contrast of max projected whole cell sections. The schematic under each image indicates the modifications on End4p, and fluorescent tags are omitted for clarity.

Reference

1. Lancaster, A. K., Nutter-Upham, A., Lindquist, S. & King, O. D. PLAAC: a web and command-line application to identify proteins with prion-like amino acid composition. *Bioinformatics* **30**, 2501–2502 (2014).